Necrosis drives susceptibility to *Mycobacterium tuberculosis* in POLG mtDNA mutator mice

Mabry CJ[1], Weindel CG[1], Stranahan LW[2], Martinez EL[1,3], VanPortfliet JJ[1,4], West AP[1,4], Patrick KL[1,5], Watson RO[1,3#]

[1]Department of Microbial Pathogenesis and Immunology, Texas A&M Health, College of Medicine, Bryan, TX 77807, USA

[2]Department of Veterinary Pathobiology, Texas A&M College of Veterinary Medicine and Biomedical Sciences, College Station, TX 77843, USA

[3]Department of Medicine, Division of Infectious Diseases, Vanderbilt University Medical Center, Nashville, TN 37232

[4]The Jackson Laboratory, Bar Harbor, Maine 04609, USA

[5]Department of Pathology, Microbiology, and Immunology, Vanderbilt University Medical Center, Nashville, TN 37232

Running head: POLG mutant mice are susceptible to *M. tuberculosis*

[#]Address Correspondence to Robert O. Watson (robert.watson@tamu.edu or robert.o.watson@vumc.org)

ABSTRACT

The genetic and molecular determinants that underlie the heterogeneity of *Mycobacterium tuberculosis* (Mtb) infection outcomes in humans are poorly understood. Multiple lines of evidence demonstrate that mitochondrial dysfunction can exacerbate mycobacterial disease severity and mutations in some mitochondrial genes confer susceptibility to mycobacterial infection in humans. Here, we report that mutations in mitochondria DNA (mtDNA) polymerase gamma (POLG) potentiate susceptibility to Mtb infection in mice. POLG mutator mtDNA mice fail to mount a protective innate immune response at an early infection timepoint, evidenced by high bacterial burdens, reduced M1 macrophages, and excessive neutrophil infiltration in the lungs. Immunohistochemistry reveals signs of enhanced necrosis in the lungs of Mtb-infected POLG mice and POLG mutator macrophages are hyper-susceptible to extrinsic triggers of necroptosis *ex vivo*. By assigning a role for mtDNA mutations in driving necrosis during Mtb infection, this work further highlights the requirement for mitochondrial homeostasis in mounting balanced immune responses to Mtb.

INTRODUCTION

Defects in mitochondria are associated with a variety of human diseases and metabolic disorders (1). Inherited mitochondrial diseases, caused by mutations harbored in the mitochondrial genome (mtDNA) or in nuclear-encoded mitochondrial genes, lead to devastating neurodegenerative and cardiovascular disorders (2). They are also frequently associated with chronic inflammation and autoimmunity. Type I interferonopathies, for example, are often caused by mutations that result in aberrant release of mitochondrial nucleic acids and chronic engagement of cytosolic nucleic acid sensing (3-5). Consistent with important links between mitochondrial health and immune function, patients with mitochondrial mutations are prone to frequent viral and bacterial infections that are often more severe (6-7). They can also suffer from systemic inflammatory response syndrome (SIRS) caused by hyper-inflammation in the absence of infection (8). Furthermore, human SNPs in mitochondrial genes have shown to confer susceptibility to several bacterial pathogens, including *Salmonella typhi* (9), *Listeria monocytogenes* (10), and *Mycobacterium leprae* (11). Despite clear connections between mitochondria and immunity, the mechanistic contributions of specific mitochondrial-associated mutations in driving susceptibility to infection remains unclear.

Mycobacterium tuberculosis (Mtb) is the causative agent of tuberculosis, an ancient disease that remains the number one infectious disease killer worldwide (12). The success of Mtb is driven in large part by its ability to manipulate and establish a replicative niche in host innate immune cells, primarily macrophages (13). A key hub in the Mtb-macrophage host-pathogen interface are mitochondria, which control cellular energetics, lipid metabolism, and the generation of reactive oxygen species, as well as gatekeep entry into programmed cell death (14). While the precise molecular determinants of TB disease severity remain elusive, decades of research have identified a role for cell death in dictating TB disease outcomes. Apoptosis, or “immunologically silent” cell death correlates with protection, whereas necrotic forms of cell death are associated with mycobacterial cell-to-cell spread and immunopathology (15). Consequently, TB has evolved a variety of strategies to inhibit apoptosis while promoting necrosis (16).

Several studies have mechanistically shown how distinct flavors of necrosis (e.g. inflammasome-mediated pyroptosis, RIPK-dependent necroptosis, ferroptosis) promote Mtb pathogenesis (17-21). We and others have begun to link cell death during Mtb infection with disruptions in mitochondrial homeostasis (14, 22-23). We recently reported that mutations in the mitochondrial-associated protein leucine-rich repeat kinase 2 (LRRK2) can promote necroptosis during Mtb infection by rendering mitochondrial membranes susceptible to damage by the pore-forming protein gasdermin D, resulting in the release of mitochondrial ROS (23). Building on this finding, we set out to determine how other mitochondrial mutations alter Mtb infection outcomes.

Here, we investigate how Mtb infection proceeds in a common model of mitochondrial dysfunction, the POLG mtDNA mutator mouse. These knock-in mice contain a D257A substitution in the proofreading exonuclease domain that results in accumulation of mtDNA mutations as the mice age (24). Although this mouse model does not harbor a specific human disease-associated mutation, it presents with symptoms that parallel many of the clinical manifestations seen in mitochondrial disease patients, such as cardiomyopathy, progressive hearing loss, and anemia (25). These mice also have exacerbated inflammatory responses and are susceptible to septic shock, which correlates with clinical symptoms seen in mitochondrial disease patients (3). Here, we report that POLG mtDNA mutator mice display enhanced susceptibility to Mtb infection evidenced by higher bacterial burdens, excessive neutrophil infiltration in the lung, and enhanced necrosis. These findings argue that mtDNA fidelity is required to maintain balanced cell death outcomes during Mtb infection.

RESULTS

POLG mutator mice harbor higher Mtb bacterial burdens

To better understand how mitochondrial-associated gene mutations drive Mtb infection outcomes, we chose to study the POLG mutator mouse model (B6.129S7(Cg)-Pol-g^{tm1Prol}/J). Because they harbor a D257A substitution in the proofreader exonuclease domain of mtDNA polymerase gamma, these mice accumulate mtDNA mutations (24). They have been a useful tool for studying mitochondrial dysfunction in aging (24, 26), but only a few studies have used them to study infection (27). Using a low-dose aerosol model, which administers 100-200 Mtb bacilli into the lungs of each animal, we infected WT and *Polg*^{D257A} mutator mice at approximately 3 months of age (**Figure 1A**). We chose to infect young mice to avoid variability in mtDNA instability and the potential for inflammation-associated pathology in our cohort (*Polg*^{D257A} mutator mice experience premature aging and early death (24, 26, 28)). At 21 days post-infection, we sacrificed mice, homogenized a portion of the lungs, spleen, and liver and enumerated Mtb colony-forming units (CFUs) to measure bacterial burden. We observed a significant increase (half-log) in Mtb recovered from the lungs of *Polg*^{D257A} mutator mice compared to WT mice (**Figure 1B**). *Polg*^{D257A} mutator mice were also more permissive to Mtb dissemination, as bacterial burdens were higher in the spleens and livers as well (**Figure 1C-D**). These findings demonstrate that mice experiencing POLG-dependent mitochondrial dysfunction cannot properly control Mtb replication and spread *in vivo*.

POLG mutator mice lungs exhibit increased neutrophils and fewer M1 macrophages during Mtb infection

Previous studies have linked POLG-related mitochondria dysfunction to elevated inflammatory responses (e.g. type I IFN) following exposure to pattern recognition receptor (PRR) agonists such as LPS and dsDNA (3). To grossly examine the inflammatory state of the lungs in Mtb-infected *Polg*^{D257A} mutator mice, we evaluated lung tissues via hematoxylin and eosin (H&E) staining. As is characteristic of Mtb infection, we observed histiocytic inflammation (aggregation of monocyte- and macrophage-derived cells) in the lungs of both genotypes (**Figure 2A-B, S2A-B**). Curiously, despite harboring higher bacterial loads, *Polg*^{D257A} mutator mice displayed less histiocytic lung inflammation at

135 day 21 post-infection compared to WT (**Figure 2C,** black outline in H&E images). This
136 suggests that *Polg*^{D257A} mutator mice fail to effectively recruit one or more types of im-
137 mune cells into infected regions of the lung. In contrast, we found that *Polg*^{D257A} mutator
138 mice lungs were more prone to neutrophil cluster formation, a phenomenon associated
139 with NET release and pathogen clearance (28,29) (**Figure 2D,** white outline in H&E im-
140 ages). These findings argue that an altered immune cell landscape dominates the lungs
141 of *Polg*^{D257A} mutator mice during Mtb infection.
142
143 To further define innate immune cell populations in the lungs of *Polg*^{D257A} mutator mice
144 during Mtb infection, we isolated single cell suspensions and used flow cytometry to
145 identify key cell types. Overall, we measured similar numbers of hematopoietic cells
146 (CD45^{+}) in the lungs of Mtb-infected *Polg*^{D257A} mutator and WT mice (**Figure 2SC**).
147 However, the percentage of total monocytes, in particular classical Ly6C^{+} CD43^{-} mono-
148 cytes, was higher in *Polg*^{D257A} mutator mice (**Figure S2D-F and 2E**). Previous studies
149 have correlated CD43 with control of Mtb in macrophages, and in mice, the absence of
150 CD43 leads to increased bacterial load and defective granuloma formation (30). We did
151 not observe major differences in the percentage of monocyte-derived macrophages
152 (CD45^{+} CD11b^{+} Ly6C^{-} SSC^{hi}) (**Figure 2SG**), dendritic cells (CD45^{+} CD11b^{+} CD11c^{+})
153 (**Figure 2SH**), or alveolar macrophages (CD45^{+} CD11b$^{low/neg}$ CD11c^{+} CD170^{+}) (**Figure**
154 **2SI**).
155
156 Consistent with the lower levels of histiocytic inflammation (**Figure 2C**), we measured
157 fewer M1 macrophages (CD86^{+} macrophages) in Mtb-infected *Polg*^{D257A} mutator mice
158 (**Figure 2F**). This was a concomitant with increased percentage of M0 (CD86^{-} CD206^{-})
159 macrophages (**Figure 2G**), supportive of a macrophage polarization defect in *Polg*^{D257A}
160 mutator mice. M2 (CD86^{-} CD206^{+}) macrophages were similar between the two geno-
161 types (**Figure 2SJ**). Importantly, pro-inflammatory M1 macrophages play an important
162 role in the early control of Mtb by promoting granuloma formation, triggering T cell infil-
163 tration, and upregulating antimicrobial molecules like nitric oxide (31-33). Concomitant
164 with fewer M1 macrophages, we observed a significant increase in the recruitment of
165 neutrophils (CD45^{+} C220^{-} CD11b^{+} Ly6G^{+}) in *Polg*^{D257A} mice lungs (**Figure 2H**).

166 Enhanced neutrophil recruitment has been previously shown in animal models and tu-
167 berculosis patients to correlate with tissue damage and poor Mtb infection outcomes
168 (34-36). Collectively, these results suggest that a combination of defective M1 macro-
169 phage polarization, low expression of CD43 on monocytes, and/or enhanced neutrophil
170 infiltration result in higher Mtb bacterial burdens in *Polg*^{D257A} mice.
171

172 **Decreased M1 macrophage responses drive susceptibility to Mtb infection in**
173 **POLG mutator mice**

174 Having observed changes in the numbers and types of cells that infiltrate *Polg*^{D257A}
175 lungs, we next wanted to compare the overall cytokine milieu of *Polg*^{D257A} and WT lungs
176 during Mtb infection. Consistent with fewer M1 macrophages, key pro-inflammatory and
177 antimicrobial transcripts including *Tnfa*, *Nos2, Ifng, Nlrp3* were reduced in *Polg*^{D257A} mu-
178 tator mice lungs *(***Figure 3A-D)**. M1 macrophage chemokine transcripts, *Cxcl9* and
179 *Cxcl10*, were also reduced in *Polg*^{D257A} mutator mice lungs (**Figure 3E-F**). *Polg*^{D257A} mu-
180 tator mice did not show differences in ISG transcripts (**Figure 5SC-E**). These data pro-
181 vide additional evidence that *Polg*^{D257A} mutator mice fail to mount a sustained inflamma-
182 tory response sufficient to control Mtb replication and dissemination.
183

184 **Necrotic debris dominates POLG mutator mouse lungs during Mtb infection**

185 Having seen altered immune cell infiltration and inflammatory transcript abundance in
186 Mtb-infected *Polg*^{D257A} mutator mice, we next looked more carefully at immunopathology
187 in the lungs.
188 We and others have previously associated necrotic debris, characterized by neutrophil
189 clusters with granular debris, with poor tuberculosis outcomes in mice (23, 37). Accord-
190 ingly, we observed increased clusters of necrotic debris in Mtb-infected *Polg*^{D257A} muta-
191 tor mice lungs compared to WT (**Figure 4A-C, white outline areas**). Because necrosis
192 is associated with exuberant Mtb growth and virulence (19, 38-39), we next used acid-
193 fast staining to look for Mtb bacilli in areas of consolidated inflammatory infiltrates. In ar-
194 eas of neutrophil clusters and necrotic debris, we qualitatively observed more clumps of
195 Mtb bacilli in *Polg*^{D257A} mutator mice lungs (**Figure 5A-B, black arrowheads**). We also
196 denoted instances of growth characteristic of cording, a virulence-related form of Mtb

growth associated with necrosis, specifically in the lungs of *Polg*^{D257A} mutator mice (**Figure 5B, white arrowheads**) (19, 38-39). These findings suggest that areas of necrotic debris that dominate *Polg*^{D257A} mutator mice lungs correlate with a failure to restrict Mtb growth.

Polg^{D257A} macrophages are prone to necrotic death and cell death in response to Mtb infection

To better understand the molecular mechanisms underlying the susceptibility of *Polg*^{D257A} mutator, we asked if their propensity to accumulate necrotic debris was due entirely to the inflammatory milieu of the lung, or if there was a cell-intrinsic propensity for *Polg*^{D257A} macrophages to undergo necrosis. To test this, we isolated bone marrow and differentiated macrophages from WT and *Polg*^{D257A} mutator mice at either 6 or 12 months of age. These ages represent the typical “onset” and “late” stages of mitochondrial disease in *Polg*^{D257A} mutator mice as they relate to human patients (24, 40). We first infected WT and *Polg*^{D257A} BMDMs from 6-month-old mice with Mtb (MOI=5) and tracked cell death kinetics using propidium iodide (PI). After 24h of infection, *Polg*^{D257A} macrophages underwent higher Mtb-induced cell death compared to WT controls (**Figure 6A**). Because Mtb infection triggers several cell death pathways in macrophages (apoptosis (41), ferroptosis (21), and inflammasome-mediated pyroptosis (17-18)) and PI cannot distinguish between these forms of cell death, we next employed canonical cell death triggers to gain additional insight into the type of cell death that is enhanced in *Polg*^{D257A} BMDMs. To begin, we treated WT and *Polg*^{D257A} BMDMs from 6-month-old mice with the apoptosis inducer staurosporine, a protein kinase inhibitor that triggers apoptosis via aberrant caspase activation. In response to a low dose of staurosporine (100 nm), we observed slightly more propidium iodide incorporation in *Polg*^{D257A} BMDMs (**Figure 6B**). These findings are consistent with previous work that found increased apoptotic markers associated with accelerated aging in POLG mutator mice (24). Next, to induce necroptosis, we treated WT and *Polg*^{D257A} BMDMs with recombinant murine TNFα in combination with a SMAC mimetic and pan-caspase inhibitor to initiate RIPK1/RIPK3/MLKL-dependent necroptosis (42). *Polg*^{D257A} macrophages isolated from 6-month-old mice were highly susceptible to necroptosis (**Figure 6C**) and this

228 phenotype was enhanced in *Polg*^{D257A} BMDMs from 12-month-old mice (**Figure 6D**).
229 These findings suggest that *Polg*^{D257A} macrophages are more sensitized to necrotic
230 forms of cell death, which may account for enhanced necrosis and Mtb dissemination *in*
231 *vivo*.
232
233 **Discussion**
234 Because mitochondrial-associated mutations can increase the risk of life-threatening in-
235 fections, there is a critical need to understand how altered mitochondrial homeostasis
236 affects the immune response to pathogens. Here, we describe how a mutation in mito-
237 chondrial POLG, which results in the accumulation of mtDNA mutations and mtDNA in-
238 stability, confers susceptibility to Mtb infection by enhancing necrosis. We demonstrate
239 that in response to Mtb, *Polg*^{D257A} mutator mice fail to mount protective immune re-
240 sponses in the lung. We propose this stems in large part from the propensity of
241 *Polg*^{D257A} macrophages to preferentially undergo necrosis over other forms of pro-
242 grammed cell death when infected with Mtb. Enhanced necrosis is a likely driver for the
243 pro-bacterial cellular immune milieu (high neutrophils, low M1 macrophages) we ob-
244 serve in *Polg*^{D257A} mutator mice. It may also directly support high levels of Mtb growth in
245 *Polg*^{D257A} lungs. Studies from the Ramakrishnan lab have repeatedly linked necrosis to
246 extracellular mycobacterial cording and poor disease outcomes in the zebrafish model
247 (43,44). In human macrophages, Mtb replication is enhanced in cells undergoing late
248 stages of necrosis that exhibit evidence of plasma membrane damage (45). Mtb has
249 also been shown to thrive in macrophages that have phagocytosed Mtb-infected PMNs
250 that died via necrosis (38). Although we were unable to decisively assess whether Mtb
251 bacilli in *Polg*^{D257A} lungs were extracellular due to limitations of H&E and AFB staining,
252 our data convincingly correlate enhanced necrosis in *Polg*^{D257A} mutator mice with high
253 Mtb bacterial burdens.
254
255 Over the course of these studies, we were surprised to find that several pro-inflamma-
256 tory cytokines and chemokines are less abundant in *Polg*^{D257A} mutator mice, despite
257 their harboring more bacteria (**Figure 3 and S3**). It is possible that the accumulation of
258 mtDNA mutations and chronic stimulation of pattern recognition receptors by

mitochondrial DAMPs render *Polg*^{D257A} immune cells refractory to immune signaling upon pathogen sensing (46). We previously reported a phenotype like this in LRRK2 KO macrophages, which have high basal type I IFN expression and are unable to induce ISG expression in response Mtb (47). It is also possible that the failure of *Polg*^{D257A} mutator mice to upregulate pro-inflammatory cytokines stems from rewiring of cellular metabolism and mitochondrial OXPHOS, which is uniquely regulated in Mtb-infected macrophages (48,49). Notably, *Polg*^{D257A} mutator mice do not always fail to induce type I IFN in response to bacterial pathogens. Recent work from the West lab shows that 48h post-intratracheal instillation of *Pseudomonas aeruginosa* strain O1 (PAO1), *Polg*^{D257A} mutator mice exhibit elevated levels of ISGs in the lung and BAL fluid (27). It is possible that upon initial encounter with Mtb, *Polg*^{D257A} mutator mice similarly hyperinduce ISGs and pro-inflammatory cytokines and that we are reporting on a different, chronic response 21 days post-infection. However, it is also possible that the *Polg*^{D257A} mutation responds to and elicits an immune milieu to different pathogens in different ways. Indeed, we know that *Pseudomonas* and Mtb initially elicit type I IFN expression through distinct signaling pathways (TLR4/TRIF (50) and cGAS (51), respectively) and likely interface with mitochondria in distinct ways as well. Investigations of Mtb-infected *Polg*^{D257A} mutator mice at additional early time points may help us distinguish between these two potential explanations.

These studies were motivated, in part, by several genome wide association studies (GWAS) that identified SNPs in mitochondrial genes that confer susceptibility to mycobacterial infection in humans. Most of these studies looked at patients with leprosy, which is caused by *Mycobacterium leprae*, a close cousin of Mtb. Mutations in genes like *Park2*, which encodes the mitophagy factor Parkin (52,53), *Tfam*, which encodes a histone-like protein of the mitochondrial genome (11), as well as *Polg* (11) have been linked to leprosy susceptibility or severity of disease. The Mtb phenotype we report is consistent with GWAS that identified a human SNP in POLG associated with multibacillary leprosy—a form of the disease characterized by high bacterial loads in lesions (11). Collectively, our study bolsters confidence in these GWAS and provides new insight into

289 the potential mitochondria-associated mechanisms driving altered susceptibility to my-
290 cobacterial disease.
291
292 Limitations of the study: One drawback of the *Polg*^{D257A} mutator mouse model is that the
293 mice accumulate mutations throughout the entire mtDNA genome over time (54). Thus,
294 one cannot ascribe pathological phenotypes to a specific defect in a single mitochon-
295 drial gene. Likewise, although human patients with mutations in the exonuclease "proof-
296 reading" domain of POLG have been linked to diseases such as Alpers and Leigh syn-
297 drome (55, 56), *Polg*^{D257A} mutator mice do not mirror a specific model of mitochondria
298 diseases. Given these caveats, future investigations may wish to probe Mtb pathogene-
299 sis in mice that more accurately model mitochondrial mutations in humans. Regardless,
300 our study adds to a growing literature arguing that mitochondrial health is required to
301 generate protective immune responses to Mtb. Accordingly, we propose that disruption
302 to mitochondrial homeostasis, via mutation, metabolic disease, stress, etc. plays a criti-
303 cal role in dictating the spectrum of tuberculosis disease in humans.
304
305 **Acknowledgements**
306 We would like to thank the members of the Watson and Patrick labs for their critical re-
307 view and feedback in the preparation of this manuscript. Funding was provided by
308 NIH/NIAID to R.O.W. and K.L.P. (R01AI155621), NIH/NIAID to C.J.M. (F31AI176795),
309 NIH training grant T32GM135748 to E.L.M., and the Parkinson's Foundation Launch
310 Award PF-Launch-938138 (C.G.W.).
311
312 **Author contributions**
313 Conceptualization, C.J.M., K.L.P., and R.O.W.; Investigation, C.J.M., C.G.W., L.W.S.,
314 E.L.M., J.J.V., A.R.W., K.L.P, and R.O.W.; Methodology, C.J.M, C.G.W., L.W.S.,
315 E.L.M., K.L.P., and R.O.W.; Visualization, C.J.M., K.L.P, and R.O.W.; Writing, C.J.M.,
316 K.L.P., and R.O.W.; Supervision, R.O.W. and K.L.P.
317
318 **Competing interests**
319 The authors declare no competing interests.

320

321 **MATERIALS and METHODS**

322 **Mouse husbandry and strains**

323 *POLG*$^{D257A/D257A}$ C57BL/6J mutator mice were purchased from the Jackson laboratory.
324 *POLG*$^{D257A/+}$ breeder pairs used to generate *POLG*$^{+/+}$ and *POLG*$^{D257A/D257A}$ experimental
325 mice were obtained from male *POLG*$^{D257A/+}$ to female C57BL/6J crosses. All mice used
326 in experiments were compared to age- and sex- matched controls and fed 4% standard
327 chow. Littermate controls were used in all experiments. For *ex vivo* BMDM experiments,
328 male mice 6-month and 12-month of age were used. For *in vivo* Mtb infections, mice
329 were infected at 12 weeks of age. All animals were housed, bred, and studied at Texas
330 A&M Health Science Center under approved Institutional Care and Use Committee
331 guidelines.

332

333 ***M. tuberculosis***

334 The Erdman strain was used for all *M. tuberculosis* infections. Low passage lab stocks
335 were thawed for each experiment to ensure virulence was preserved. *M. tuberculosis*
336 was cultured in roller bottles at 37°C in Middlebrook 7H9 broth (BD Biosciences) supple-
337 mented with 10% OADC (BD Biosciences), 0.5% glycerol (Fisher), and 0.1% Tween-80
338 (Fisher) or on 7H10 plates. All work with *M. tuberculosis* was performed under Biosafety
339 level 3 containment using procedures approved by the Texas A&M University Institu-
340 tional Biosafety Committee.

341

342 **Primary cell culture**

343 Bone marrow derived macrophages (BMDMs) were isolated by flushing mouse femurs
344 and tibias with 10 mL DMEM 1 mM sodium pyruvate. Cell suspensions were centrifuged
345 at 400 rcf for 5 min and responded in BMDM media (DMEM, 20% FBS (MilliporeSigma),
346 1 mM sodium pyruvate (Lonza), 10% MCSF conditioned media (Watson lab)). Cells
347 were plated on non-TC treated plates and differentiated at 37°C 5% CO_2. On day 3 fol-
348 lowing plating, cells were fed 50% additional volume with BMDM media. Cells were har-
349 vested at day 7 with 1XPBS EDTA (Lonza).

350

351 **METHOD DETAILS**

352 ***M. tuberculosis* infection**

353 For *M. tuberculosis* infections *ex vivo*, low passage Mtb was prepared by growing it to
354 log phase (OD600 0.6-0.8). Bacterial cultures were spun at 58 rcf for 5 min to remove
355 large clumps. The bacteria was then pelleted at 2103 rcf for 5 min and washed with
356 1XPBS. The wash step was repeated twice. The resuspended bacteria cultures were
357 sonicated at 70% amplitude for 10 sec repeated three times (Branson Ultrasonics
358 Corp.) followed by a low speed spin (58 rcf) to remove remaining clumps. The bacteria
359 were diluted in DMEM (Hyclone) + 10% horse serum (Gibco) for *ex vivo* infections, or
360 1X PBS for *in vivo* infections. For *ex vivo* infections, plates containing cells and bacteria
361 were spun at 234 rcf for 10 min to synchronize infection. Fresh BMDM media was then
362 added to the cells. See "plate based assays for cell death" for details on measuring cell
363 death kinetics during Mtb infection.

364

365 **Plate based assays for cell death**

366 BMDMs were plated in 96-well clear bottom plates (Corning) at $2.5x10^4$ cells/well in 50
367 μL of media. Following cell adherence (1 hr), an additional 25 μL was added to each
368 well. The following day, media was removed, and respective agonists were used to initi-
369 ate various cell death modalities. For cell death assays, 5 μg/ml propidium iodide (PI)
370 (ThermoFisher) was added at the time of adding cell death agonists. Total cell numbers
371 used for normalization were counted on a subset of cells using NucBlue (ThermoFisher)
372 in 1X PBS. Live cell imaging was done using 4X magnification on either a Lionheart
373 plate reader or Cytation 5 (Biotek). Post-run analysis was conducted using Gen5 v3.15
374 (Biotek) software. For necroptosis induction, cells were activated with 100 ng/ml recom-
375 binant murine TNFα (PeproTech), 500 nM SMAC mimetic birinapant (Selleck Chemi-
376 cals), and 20 μM pan-caspase inhibitor z-VAD-FMK (R&D Systems). Apoptosis was in-
377 duced with 100 nM stauroporine (Tocris Bioscience).

378

379 ***In vivo* Mtb infections**

380 All infections were performed using procedures approved by Texas A&M University In-
381 stitutional Care and Use Committee. The Mtb inoculum was prepared as described

382 above. Age- and sex-matched mice were infected via inhalation exposure using a Madi-
383 son chamber (Glas-Col) calibrated to introduce 100-200 CFUs per mouse. For each in-
384 fection, approximately 3 mice were euthanized immediately, and their lungs were ho-
385 mogenized and plated to verify an accurate inoculum. Infected mice were housed under
386 BSL3 containment and monitored daily by lab members and veterinary staff. At the indi-
387 cated time points, mice were euthanized, and tissue samples were collected. Blood was
388 collected in serum collection tubes, allowed to clot for 1-2 hrs at RT, and spun at 1000
389 rpm for 10 min to separate serum. Organs were divided to maximize infection readouts
390 (CFUs: left lobe lung and 1⁄2 spleen; histology: 2 right lung lobes and 1⁄4 spleen; RNA:
391 post-caval lobe and 1⁄4 spleen; Flow: right inferior lobe). For histological analysis organs
392 were fixed for 24 hrs in 10% neutral buffered formalin and moved to ethanol (lung,
393 spleen). Organs were further processed as described below. For cytokine transcript
394 analysis, organs were homogenized in Trizol, and RNA was isolated as described be-
395 low. For CFU enumeration, organs were homogenized in 5 ml PBS + 0.1% Tween-80,
396 and serial dilutions were plated on 7H10 plates. Colonies were counted after plates
397 were incubated at 37°C for 3 weeks.
398
399 **Gene expression analysis by RT-qPCR**
400 For lung tissue, RNA was isolated using Direct-zol RNAeasy kits (Zymogen). cDNA was
401 synthesized with Bio-Rad iScript Direct Synthesis kits (BioRad) per manufacturer's pro-
402 tocol. RT-qPCR was performed in triplicate wells using PowerUp SYBR Green Master
403 Mix. Data was analyzed on a QuantStudio 6 Real-Time PCR System (Applied Biosys-
404 tems), and quantification of gene expression was performed using a standard curve and
405 normalized to *Actb* expression levels. qRT-PCR primer sequences can be found in **Ta-**
406 **ble 1**.
407
408 **Flow cytometry**
409 For *ex vivo* analysis of lung cell populations at 21 days post Mtb infection, the right infe-
410 rior lobe was isolated and washed twice in 1X PBS. The lung was then minced and di-
411 gested in digestion buffer (70 μg/ml Liberase (Roche) and 50 μg/ml DNASE I (manufac-
412 turer) in RPMI 1640 (HyClone)) for 30 min at 37°C 5% CO_2. Single suspensions were

413 achieved by consecutively filtering homogenates through 70 μM and 40μM cell strain-
414 ers. Live dead staining was performed using Ghost dye 510 (Tonbo). Fc receptors were
415 blocked using CD16/CD32 monoclonal antibody (eBiosciences). Cells were stained with
416 antibodies against surface proteins CD11b (BV421, BDBiosciences), CD11c (BV605,
417 BioLegend), CD45 (BV785, BioLegend), CD170 (eFluor-488, eBiosciences), CD43 (PE,
418 BD Biosciences), Ly6G (PerCP-Cy5.5, eBiosciences), Ly6C (APC, eBiosciences),
419 CD206 (APCeFLuor-700 eBiosciences), CD86 (APCeFluor-780, eBiosciences). Cells
420 were washed 2 times before fixing in 4% PFA for 15 min at RT. Following fixation cells
421 were washed twice with 1X PBS and incubated overnight at 4°C. Total lung cell counts
422 were based on live single cells (Ghost low/-) in 200 mL or 1/3 lung lobe. FSC/SSC was
423 used to differentiate macrophage ($CD45^{+}$ $CD11b^{+}$ $Ly6G^{-}$ $CD11c^{low/-}$ SSC^{hi} FSC^{mid}) and
424 monocyte (($CD45^{+}$ $CD11b^{+}$ $Ly6G^{-}$ $CD11c^{low/-}$ SSC^{lo} FSC^{mid}) Flow cytometry was per-
425 formed on the LSR Fortessa X20, and FCS Express software was used for post-acquisi-
426 tion analysis.
427
428 **Histopathology**
429 Mtb infected mouse lungs were fixed with 10% neutral formalin and processed, embed-
430 ded in paraffin, and cut into 5 μM sections and stained with hematoxylin and eosin
431 (H&E) or acid-fast stain (AFB) (AML Laboratories). A boarded veterinary pathologist
432 performed a blinded evaluation of lung sections for inflammation. To quantify the per-
433 centage of lung fields occupied by histiocytic inflammatory infiltrates, scanned images of
434 a lobe of each lung were analyzed using QuPath Bioimage analysis v 0.4.3 to determine
435 the total cross-sectional area of inflammatory foci per total lung cross sectional area.
436 Additional criteria were evaluated by dividing the digital images into 500 × 500 μm grids
437 and counting the percentage of squares containing neutrophils, neutrophils arranged in
438 clusters (> 5 neutrophils in close approximation), or degenerate neutrophils/necrotic cel-
439 lular debris.
440
441 **Statistical analysis**
442 All data are representative of two or more independent experiments with n=3 or greater
443 unless specifically noted in the figure legends. For all quantifications, n represents the

number of biological replicates, either number of wells containing cells or number of mice. Error bars represent SEM. For *in vitro* assays, statistical significance was determined using either a two-tailed Student's unpaired T test or two-way ANOVA with Tukey's post hoc test. For *in vivo* mouse infections, significance was determined using a Mann-Whitney U test based on the assumption that samples (mice) followed a non-normal distribution. The specific statistical test used to determine significance for each experiment is listed at the end of the figure legends. All calculations of significance were determined using GraphPad Prism Version 10 Software expressed as P values. The threshold for significance was determined by a p value of < 0.05, and annotated as * = $p<0.05$, ** = $p<0.01$, *** = $p<0.001$, ****=$p<0.0001$. For *in vivo* infection mouse experiments, we estimated that detecting a significant effect requires two samples to differ in CFUs by 0.7e^10. Using a standard deviation of 0.3e^10 for each population, we calculated that a minimum size of 5 age- and sex-matched mice per group per time point is necessary to detect a statistically significant difference by a t-test with alpha (2-sided) set at 0.05 and a power of 80%. Therefore, we used a minimum of 5 mice per genotype per time point to assess infection-related readouts.

472 **REFERENCES**

473 1. Zong Y, Li H, Liao P, Chen L, Pan Y, Zheng Y, Zhang C, Liu D, Zheng M, Gao J.
474 2024. Mitochondrial dysfunction: mechanisms and advances in therapy. Signal Trans-
475 duct Target Ther 9:124.
476 2. Rusecka J, Kaliszewska M, Bartnik E, Tońska K. 2018. Nuclear genes involved
477 in mitochondrial diseases caused by instability of mitochondrial DNA. J Appl Genet
478 59:43–57.

479 3. Lei Y, Guerra Martinez C, Torres-Odio S, Bell SL, Birdwell CE, Bryant JD, Tong
480 CW, Watson RO, West LC, West AP. 2021. Elevated type I interferon responses poten-
481 tiate metabolic dysfunction, inflammation, and accelerated aging in mtDNA mutator
482 mice. Sci Adv 7:eabe7548.

483 4. West AP, Khoury-Hanold W, Staron M, Tal MC, Pineda CM, Lang SM, Bestwick
484 M, Duguay BA, Raimundo N, MacDuff DA, Kaech SM, Smiley JR, Means RE, Iwasaki
485 A, Shadel GS. 2015. Mitochondrial DNA stress primes the antiviral innate immune re-
486 sponse. Nature 520:553–557.

487 5. Warren EB, Gordon-Lipkin EM, Cheung F, Chen J, Mukherjee A, Apps R, Tsang
488 JS, Jetmore J, Schlein ML, Kruk S, Lei Y, West AP, McGuire PJ. 2023. Inflammatory
489 and interferon gene expression signatures in patients with mitochondrial disease. J
490 Transl Med 21:331.

491 6. Edmonds JL, Kirse DJ, Kearns D, Deutsch R, Spruijt L, Naviaux RK. 2002. The
492 otolaryngological manifestations of mitochondrial disease and the risk of neurodegener-
493 ation with infection. Arch Otolaryngol Head Neck Surg 128:355–362.

494 7. Eom S, Lee HN, Lee S, Kang H-C, Lee JS, Kim HD, Lee Y-M. 2017. Cause of
495 Death in Children With Mitochondrial Diseases. Pediatr Neurol 66:82–88.

496 8. Walker MA, Slate N, Alejos A, Volpi S, Iyengar RS, Sweetser D, Sims KB, Walter
497 JE. 2014. Predisposition to infection and SIRS in mitochondrial disorders: 8 years' expe-
498 rience in an academic center. J Allergy Clin Immunol Pract 2:465–468, 468.e1.

499 9. Chen H-Y, Hsieh W-C, Liu Y-C, Li H-Y, Liu P-Y, Hsu Y-T, Hsu S-C, Luo A-C, Kuo
500 W-C, Huang Y-J, Liou G-G, Lin M-Y, Ko C-J, Tsai H-C, Chang S-J. 2024. Mitochondrial
501 injury induced by a Salmonella genotoxin triggers the proinflammatory senescence-as-
502 sociated secretory phenotype. Nat Commun 15:2778.

503 10. Spier A, Connor MG, Steiner T, Carvalho F, Cossart P, Eisenreich W, Wai T,
504 Stavru F. 2021. Mitochondrial respiration restricts Listeria monocytogenes infection by
505 slowing down host cell receptor recycling. Cell Rep 37:109989.

506 11. Wang D, Li G-D, Fan Y, Zhang D-F, Bi R, Yu X-F, Long H, Li Y-Y, Yao Y-G.
507 2017. The mtDNA replication-related genes TFAM and POLG are associated with lep-
508 rosy in Han Chinese from Southwest China. J Dermatol Sci 88:349–356.

509 12. World Health Organization. 2023. Global tuberculosis report 2023. World Health
510 Organization, Geneva, Switzerland.

511 13. Sankar P, Mishra BB. 2023. Early innate cell interactions with Mycobacterium tu-
512 berculosis in protection and pathology of tuberculosis. Front Immunol 14:1260859.
513 14. Patrick KL, Watson RO. 2021. Mitochondria: Powering the Innate Immune Re-
514 sponse to Mycobacterium tuberculosis Infection. Infect Immun 89:e00687-20.

515 15. Stutz MD, Allison CC, Ojaimi S, Preston SP, Doerflinger M, Arandjelovic P,
516 Whitehead L, Bader SM, Batey D, Asselin-Labat M-L, Herold MJ, Strasser A, West NP,
517 Pellegrini M. 2021. Macrophage and neutrophil death programs differentially confer re-
518 sistance to tuberculosis. Immunity 54:1758-1771.e7.

519 16. Briken V, Miller JL. 2008. Living on the edge: inhibition of host cell apoptosis by
520 Mycobacterium tuberculosis. Future Microbiol 3:415–422.

521 17. Beckwith KS, Beckwith MS, Ullmann S, Sætra RS, Kim H, Marstad A, Åsberg
522 SE, Strand TA, Haug M, Niederweis M, Stenmark HA, Flo TH. 2020. Plasma membrane
523 damage causes NLRP3 activation and pyroptosis during Mycobacterium tuberculosis
524 infection. Nat Commun 11:2270.

525 18. Qu Z, Zhou J, Zhou Y, Xie Y, Jiang Y, Wu J, Luo Z, Liu G, Yin L, Zhang X-L.
526 2020. Mycobacterial EST12 activates a RACK1-NLRP3-gasdermin D pyroptosis-IL-1β
527 immune pathway. Sci Adv 6:eaba4733.

528 19. Roca FJ, Whitworth LJ, Redmond S, Jones AA, Ramakrishnan L. 2019. TNF In-
529 duces Pathogenic Programmed Macrophage Necrosis in Tuberculosis through a Mito-
530 chondrial-Lysosomal-Endoplasmic Reticulum Circuit. Cell 178:1344-1361.e11.

531 20. Butler RE, Krishnan N, Garcia-Jimenez W, Francis R, Martyn A, Mendum T,
532 Felemban S, Locker N, Salguero FJ, Robertson B, Stewart GR. 2017. Susceptibility of
533 Mycobacterium tuberculosis-infected host cells to phospho-MLKL driven necroptosis is
534 dependent on cell type and presence of TNFα. Virulence 8:1820–1832.

535 21. Amaral EP, Costa DL, Namasivayam S, Riteau N, Kamenyeva O, Mittereder L,
536 Mayer-Barber KD, Andrade BB, Sher A. 2019. A major role for ferroptosis in Mycobacte-
537 rium tuberculosis-induced cell death and tissue necrosis. J Exp Med 216:556–570.

538 22. Ellzey LM, Patrick KL, Watson RO. 2023. Mitochondrial reactive oxygen species:
539 double agents in Mycobacterium tuberculosis infection. Curr Opin Immunol 84:102366.

540 23. Weindel CG, Martinez EL, Zhao X, Mabry CJ, Bell SL, Vail KJ, Coleman AK,
541 VanPortfliet JJ, Zhao B, Wagner AR, Azam S, Scott HM, Li P, West AP, Karpac J, Pat-
542 rick KL, Watson RO. 2022. Mitochondrial ROS promotes susceptibility to infection via
543 gasdermin D-mediated necroptosis. Cell 185:3214-3231.e23.

544 24. Kujoth GC, Hiona A, Pugh TD, Someya S, Panzer K, Wohlgemuth SE, Hofer T,
545 Seo AY, Sullivan R, Jobling WA, Morrow JD, Van Remmen H, Sedivy JM, Yamasoba T,
546 Tanokura M, Weindruch R, Leeuwenburgh C, Prolla TA. 2005. Mitochondrial DNA mu-
547 tations, oxidative stress, and apoptosis in mammalian aging. Science 309:481–484.

548 25. Chen ML, Logan TD, Hochberg ML, Shelat SG, Yu X, Wilding GE, Tan W, Kujoth
549 GC, Prolla TA, Selak MA, Kundu M, Carroll M, Thompson JE. 2009. Erythroid dysplasia,
550 megaloblastic anemia, and impaired lymphopoiesis arising from mitochondrial dysfunc-
551 tion. Blood 114:4045–4053.

552 26. Yu T, Slone J, Liu W, Barnes R, Opresko PL, Wark L, Mai S, Horvath S, Huang
553 T. 2022. Premature aging is associated with higher levels of 8-oxoguanine and in-
554 creased DNA damage in the Polg mutator mouse. Aging Cell 21:e13669.

555 27. VanPortfliet JJ, Lei Y, Martinez CG, Wong J, Pflug K, Sitcheran R, Kneeland SC,
556 Murray SA, McGuire PJ, Cannon CL, West AP. 2024. Caspase-11 drives macrophage
557 hyperinflammation in models of Polg-related mitochondrial disease. bioRxiv
558 2024.05.11.593693.

559 28. Khazen R, Corre B, Garcia Z, Lemaître F, Bachellier-Bassi S, d'Enfert C, Bousso
560 P. 2022. Spatiotemporal dynamics of calcium signals during neutrophil cluster for-
561 mation. Proc Natl Acad Sci U S A 119:e2203855119.

562 29. Deng P, Xu A, Grin PM, Matthews K, Duffy SP, Ma H. 2024. Auto-amplification
563 and spatial propagation of neutrophil extracellular traps. Commun Biol 7:386.
564

565 30. Randhawa AK, Ziltener HJ, Merzaban JS, Stokes RW. 2005. CD43 is required
566 for optimal growth inhibition of Mycobacterium tuberculosis in macrophages and in
567 mice. J Immunol 175:1805–1812.

568 31. Khan A, Zhang K, Singh VK, Mishra A, Kachroo P, Bing T, Won JH, Mani A, Pa-
569 panna R, Mann LK, Ledezma-Campos E, Aguillon-Duran G, Canaday DH, David SA,
570 Restrepo BI, Viet NN, Phan H, Graviss EA, Musser JM, Kaushal D, Gauduin MC, Jag-
571 annath C. 2022. Human M1 macrophages express unique innate immune response
572 genes after mycobacterial infection to defend against tuberculosis. Commun Biol 5:480.

573 32. Huang Z, Luo Q, Guo Y, Chen J, Xiong G, Peng Y, Ye J, Li J. 2015. Mycobacte-
574 rium tuberculosis-Induced Polarization of Human Macrophage Orchestrates the For-
575 mation and Development of Tuberculous Granulomas In Vitro. PLoS One 10:e0129744.

576 33. Park J-H, Shim D, Kim KES, Lee W, Shin SJ. 2021. Understanding Metabolic
577 Regulation Between Host and Pathogens: New Opportunities for the Development of
578 Improved Therapeutic Strategies Against Mycobacterium tuberculosis Infection. Front
579 Cell Infect Microbiol 11:635335.

580 34. Alcantara CA, Glassman I, Nguyen KH, Parthasarathy A, Venketaraman V. 2023.
581 Neutrophils in Mycobacterium tuberculosis. Vaccines (Basel) 11:631.

582 35. Nwongbouwoh Muefong C, Owolabi O, Donkor S, Charalambous S, Bakuli A,
583 Rachow A, Geldmacher C, Sutherland JS. 2022. Neutrophils Contribute to Severity of
584 Tuberculosis Pathology and Recovery From Lung Damage Pre- and Posttreatment. Clin
585 Infect Dis 74:1757–1766.

586 36. Hult C, Mattila JT, Gideon HP, Linderman JJ, Kirschner DE. 2021. Neutrophil Dy-
587 namics Affect Mycobacterium tuberculosis Granuloma Outcomes and Dissemination.
588 Front Immunol 12:712457.

589 37. Amaral EP, Namasivayam S, Queiroz ATL, Fukutani E, Hilligan KL, Aberman K,
590 Fisher L, Bomfim CCB, Kauffman K, Buchanan J, Santuo L, Gazzinelli-Guimaraes PH,
591 Costa DL, Teixeira MA, Barreto-Duarte B, Rocha CG, Santana MF, Cordeiro-Santos M,
592 Barber DL, Wilkinson RJ, Kramnik I, Igarashi K, Scriba T, Mayer-Barber KD, Andrade
593 BB, Sher A. 2024. BACH1 promotes tissue necrosis and Mycobacterium tuberculosis
594 susceptibility. Nat Microbiol 9:120–135.

595 38. Dallenga T, Repnik U, Corleis B, Eich J, Reimer R, Griffiths GW, Schaible UE.
596 2017. M. tuberculosis-Induced Necrosis of Infected Neutrophils Promotes Bacterial
597 Growth Following Phagocytosis by Macrophages. Cell Host Microbe 22:519-530.e3.

598 39. Roca FJ, Ramakrishnan L. 2013. TNF dually mediates resistance and suscepti-
599 bility to mycobacteria via mitochondrial reactive oxygen species. Cell 153:521–534.

600 40. Trifunovic A, Wredenberg A, Falkenberg M, Spelbrink JN, Rovio AT, Bruder CE,
601 Bohlooly-Y M, Gidlöf S, Oldfors A, Wibom R, Törnell J, Jacobs HT, Larsson N-G. 2004.
602 Premature ageing in mice expressing defective mitochondrial DNA polymerase. Nature
603 429:417–423.

604 41. Behar SM, Martin CJ, Booty MG, Nishimura T, Zhao X, Gan H-X, Divangahi M,
605 Remold HG. 2011. Apoptosis is an innate defense function of macrophages against My-
606 cobacterium tuberculosis. Mucosal Immunol 4:279–287.

607 42. Akara-Amornthum P, Lomphithak T, Choksi S, Tohtong R, Jitkaew S. 2020. Key
608 necroptotic proteins are required for Smac mimetic-mediated sensitization of cholangio-
609 carcinoma cells to TNF-α and chemotherapeutic gemcitabine-induced necroptosis.
610 PLoS One 15:e0227454.

611 43. Davis JM, Ramakrishnan L. 2009. The role of the granuloma in expansion and
612 dissemination of early tuberculous infection. Cell 136:37–49.

613 44. Pagán AJ, Yang C-T, Cameron J, Swaim LE, Ellett F, Lieschke GJ, Ramakrish-
614 nan L. 2015. Myeloid Growth Factors Promote Resistance to Mycobacterial Infection by
615 Curtailing Granuloma Necrosis through Macrophage Replenishment. Cell Host Microbe
616 18:15–26.

617 45. Lerner TR, Borel S, Greenwood DJ, Repnik U, Russell MRG, Herbst S, Jones
618 ML, Collinson LM, Griffiths G, Gutierrez MG. 2017. Mycobacterium tuberculosis repli-
619 cates within necrotic human macrophages. J Cell Biol 216:583–594.

620 46. Etna MP, Giacomini E, Severa M, Coccia EM. 2014. Pro- and anti-inflammatory
621 cytokines in tuberculosis: a two-edged sword in TB pathogenesis. Semin Immunol
622 26:543–551.

623 47. Weindel CG, Bell SL, Vail KJ, West KO, Patrick KL, Watson RO. 2020. LRRK2
624 maintains mitochondrial homeostasis and regulates innate immune responses to Myco-
625 bacterium tuberculosis. Elife 9:e51071.

626 48. Cumming BM, Addicott KW, Adamson JH, Steyn AJ. 2018. Mycobacterium tuber-
627 culosis induces decelerated bioenergetic metabolism in human macrophages. Elife
628 7:e39169.

629 49. Olson GS, Murray TA, Jahn AN, Mai D, Diercks AH, Gold ES, Aderem A. 2021.
630 Type I interferon decreases macrophage energy metabolism during mycobacterial infec-
631 tion. Cell Rep 35:109195.

632 50. Jabir MS, Ritchie ND, Li D, Bayes HK, Tourlomousis P, Puleston D, Lupton A,
633 Hopkins L, Simon AK, Bryant C, Evans TJ. 2014. Caspase-1 cleavage of the TLR

634 adaptor TRIF inhibits autophagy and β-interferon production during Pseudomonas aeru-
635 ginosa infection. Cell Host Microbe 15:214–227.

636 51. Watson RO, Bell SL, MacDuff DA, Kimmey JM, Diner EJ, Olivas J, Vance RE,
637 Stallings CL, Virgin HW, Cox JS. 2015. The Cytosolic Sensor cGAS Detects Mycobac-
638 terium tuberculosis DNA to Induce Type I Interferons and Activate Autophagy. Cell Host
639 Microbe 17:811–819.

640 52. Mira MT, Alcaïs A, Nguyen VT, Moraes MO, Di Flumeri C, Vu HT, Mai CP, Ngu-
641 yen TH, Nguyen NB, Pham XK, Sarno EN, Alter A, Montpetit A, Moraes ME, Moraes
642 JR, Doré C, Gallant CJ, Lepage P, Verner A, Van De Vosse E, Hudson TJ, Abel L,
643 Schurr E. 2004. Susceptibility to leprosy is associated with PARK2 and PACRG. Nature
644 427:636–640.

645 53. Fava VM, Xu YZ, Lettre G, Van Thuc N, Orlova M, Thai VH, Tao S, Croteau N,
646 Eldeeb MA, MacDougall EJ, Cambri G, Lahiri R, Adams L, Fon EA, Trempe J-F, Cobat
647 A, Alcaïs A, Abel L, Schurr E. 2019. Pleiotropic effects for Parkin and LRRK2 in leprosy
648 type-1 reactions and Parkinson's disease. Proc Natl Acad Sci U S A 116:15616–15624.

649 54. Williams SL, Huang J, Edwards YJK, Ulloa RH, Dillon LM, Prolla TA, Vance JM,
650 Moraes CT, Züchner S. 2010. The mtDNA mutation spectrum of the progeroid Polg mu-
651 tator mouse includes abundant control region multimers. Cell Metab 12:675–682.

652 55. Saneto RP, Cohen BH, Copeland WC, Naviaux RK. 2013. Alpers-Huttenlocher
653 syndrome. Pediatr Neurol 48:167–178.

654 56. Rahman S, Copeland WC. 2019. POLG-related disorders and their neurological
655 manifestations. Nat Rev Neurol 15:40–52.

656

657

658

659

660 **Table:**

661 **Table 1: qRT-PCR primer sequences**

Gene	FWD primer	REV primer
Tnfa	ATGGCCTCCCTCTCATCAGT	GTTTGCTACGACGTGGGCTA
Nos2	GCAGCACTTGGATCAGGAA	GAAACTTCGGAAGGGAGCAA
Ifng	CTCTTCCTCATGGCTGTTTCT	CGCTTATGTTGCTGATGG
Nlrp3	AAAATGCCTTGGGAGATCCA	AAGTAAGGCCAGAATTCACC
Cxcl9	TGTGGAGTTCGAGGAACCCT	TGCCTTGGCTGGTGCTG
Cxcl10	CCAAGTGCTGCCGTCATTTTC	GGCTCGCAGGGATGATTTCAA
Il1b	GGTGTGTGACGTTCCCATTA	ATTGAGGTGGAGAGCTTTCAG
Il6	CCAGAGTCCTTCAGAGAGATACA	CCTTCTGTGACTCCAGCTTATC
Il1ra	CAGCTCATTGCTGGGTACTT	CTCAGAGCGGATGAAGGTAAAG
Isg15	GAGCTAGAGCCTGCAGCAAT	TTCTGGGCAATCTGCTTCTT
Rsad2	ATAGTGAGCAATGGCAGCCT	AACCTGCTCATCGAAGCTGT
Cxcl1	CCGAAGTCATAGCCACACTCA	CTCCGTTACTTGGGGACACC
Cxcl5	TGCCCTACGGTGGAAGTCAT	AGCTTTCTTTTTGTCACTGCCC
beta-Actin	GGTGTGATGGTGGGAATGG	GCCCTCGTCACCCACATAGGA

662

663

664

665

666

667

668

669

670

671

672

673 **Figure 1. *Polg*^{D257A} mutator mice display increased Mtb replication and dissemina-**
674 **tion *in vivo.***

675 (A) Experimental timeline of Mtb *in vivo* infection.
676 (B) Mtb colony forming units (CFUs) collect from WT and *Polg*^{D257A} mice lungs at
677 day 21 post-Mtb infection.
678 (C) CFUs recovered from WT and *Polg*^{D257A} mice spleens at day 21 post-Mtb infec-
679 tion.
680 (D) CFUs recovered from WT and *Polg*^{D257A} mice livers at day 21 post-Mtb infection.
681 Statistical analysis: *$p < 0.05$, **$p < 0.01$, ***$p < 0.001$. Statistical significance deter-
682 mined for (B-D) using Mann-Whitney test.

683
684
685
686
687
688
689
690
691
692
693
694
695
696
697
698
699
700

701 **Figure 2. *Polg*^{D257A} mutator mice display increased neutrophils and less M1 mac-**
702 **rophages during Mtb infection.**

703 (A) Hematoxylin and eosin staining of WT lungs at day 21 post-Mtb infection. Aster-
704 isks denote areas of consolidated and infiltrated by inflammatory cells. Black dashed
705 line delineates regions of healthy versus inflamed areas of lung in right panel. Outlined
706 regions (white dashed lines) in denote areas of neutrophil clusters. Upper panel scale
707 bar is 800 μM. Lower panel scale bar is 20 μM.
708 (B) As in (A) for *Polg*^{D257A} mice.
709 (C) Quantification of histiocytic inflammation using H&E staining of WT and *Polg*^{D257A}
710 mice lungs at day 21 post-Mtb infection.
711 (D) Average total surface area of neutrophil clusters using H&E staining of WT and
712 *Polg*^{D257A} mice lungs at day 21 post-Mtb infection.
713 (E) Lung CD43^{-} monocytes in WT and *Polg*^{D257A} mice analyzed by flow cytometry at
714 day 21 post-Mtb infection.
715 (F) As in (E) but for lung M1 macrophages.
716 (G) As in (E) but for lung M0 macrophages.
717 (H) As in (E) but for lung neutrophils.
718 Statistical analysis: *$p < 0.05$, **$p < 0.01$, ***$p < 0.001$. Statistical significance deter-
719 mined for (C-H) using Mann-Whitney test.
720
721
722
723
724
725
726
727
728
729
730
731

732 **Figure 2S. Cytokine analysis of *Polg*^{D257A} mutator mice lungs during Mtb infection.**

733 (A) Hematoxylin and eosin staining of WT mice lungs at day 21 post- Mtb infection.
734 Asterisks denote areas of consolidated and infiltrated by inflammatory cells. Black
735 dashed line delineates regions of healthy versus inflamed areas of lung in right panel.
736 Outlined regions (white dashed lines) in denote areas of neutrophil clusters. Upper
737 panel scale bar is 800 μM. Lower panel scale bar is 20 μM.

738 (B) As in (A) but H & E staining in *Polg*^{D257A} mice lungs at day 21 post-Mtb infection.

739 (C) Lung CD45^{+} cells in WT and *Polg*^{D257A} mice analyzed by flow cytometry at day
740 21 post-Mtb infection.

741 (D) As in (C) but for lung monocyte derived macrophages.

742 (E) As in (C) but for lung M2 macrophages.

743 (F) As in (C) but for lung myeloid dendritic cells.

744 (G) As in (C) but for lung alveolar macrophages.

745 (H) As in (C) but for lung monocytes.

746 (I) As in (C) but for lung Ly6C^{hi} CD43^{+} monocytes.

747 (J) As in (C) but for lung Ly6C^{lo} CD43^{+} monocytes.

748 Statistical analysis: *$p < 0.05$, **$p < 0.01$, ***$p < 0.001$. Statistical significance deter-
749 mined for (C-J) using Mann-Whitney test.

750

751

752

753

754

755

756

757

758

759

760

761 **Figure 3. Dampened M1 macrophage pro-inflammatory response is a hallmark of**
762 ***Polg*^{D257A} mutator mice during Mtb infection**

763 (A) Lung *Tnfa* transcripts in WT and *Polg*^{D257A} mice analyzed by qRT-PCR at day 21
764 post- Mtb infection.
765 (B) As in (A) but for *Nos2*
766 (C) As in (A) but for *Ifng*
767 (D) As in (A) but for *Nlrp3*
768 (E) As in (A) but for *Cxcl9*
769 (F) As in (A) but for *Cxcl10*
770 Statistical analysis: *$p < 0.05$, **$p < 0.01$, ***$p < 0.001$. Statistical significance deter-
771 mined for (A-F) using Mann-Whitney test.
772
773
774
775
776
777
778
779
780
781
782
783
784
785
786
787
788
789
790
791

792 **Figure 3S. *Polg*^{D257A} mutator mice do not show differences in interferon stimu-**
793 **lated genes (ISGs) during Mtb infection**

794 (A) Lung *Il1b* transcripts in WT and *Polg*^{D257A} mice analyzed by qRT-PCR at day 21
795 post- Mtb infection.
796 (B) As in (A) but for *Il6*
797 (C) As in (A) but for *Il1ra*
798 (D) As in (A) but for *Isg15*
799 (E) As in (A) but for *Rsad2*
800 (F) As in (A) but for *Cxcl1*
801 (G) As in (A) but for *Cxcl5*
802 Statistical analysis: *$p < 0.05$, **$p < 0.01$, ***$p < 0.001$. Statistical significance deter-
803 mined for (A-G) using Mann-Whitney test.
804
805
806
807
808
809
810
811
812
813
814
815
816
817
818
819
820

821 **Figure 4. *Polg*^{D257A} mutator mice exhibit increased necrotic debris during Mtb in-**
822 **fection.**

823 (A) H&E staining of WT mice lungs at day 21 post- Mtb infection. Asterisks denote
824 areas of consolidated and infiltrated by inflammatory cells. Outlined regions (white
825 dashed lines) denote areas of necrotic debris. Upper panel scale bar is 800 μM. Lower
826 panel scale bar is 20 μM.

827 (B) As in (A) but for *Polg*^{D257A} mice.

828 (C) Quantification of necrotic debris using H&E staining of WT and *Polg*^{D257A} mice
829 lungs at day 21 post-Mtb infection.

830 Statistical analysis: *$p < 0.05$, **$p < 0.01$, ***$p < 0.001$. Statistical significance deter-
831 mined for (C) using Mann-Whitney test.

832
833
834
835
836
837
838
839
840
841
842
843
844
845
846
847
848
849
850

851 **Figure 5. Higher levels of necrotic debris contribute to higher bacilli burden in**
852 ***Polg*^{D257A} mutator mice during Mtb infection.**

853 (A) H&E and acid-fast bacilli (AFB) staining of WT mice lungs at day 21 post- Mtb
854 infection. Asterisks denote areas of consolidated and infiltrated by inflammatory cells in
855 left panel. Left panel scale bar is 800 μM. Right panel scale bar is 20 μM. White arrow-
856 heads denote instances of Mtb cording. Black arrowheads denote clumps of Mtb bacilli.
857 (B) As in (A) but for *Polg*^{D257A} mice.
858
859
860
861
862
863
864
865
866
867
868
869
870
871
872
873
874
875
876
877
878
879
880

881 **Figure 6. *Polg*^{D257A} mutator macrophages are prone to necrotic cell death.**

882 (A) Cell death in 6-month-old WT and *Polg*^{D257A} macrophages infected with Mtb for
883 48h (MOI=5). Cell death was measured by propidium iodide uptake (% cell death= Pro-
884 pidium iodide positive/ total cell count *100%).
885 (B) As in (A) but 6-month-old WT and *Polg*^{D257A} macrophages were treated with 100
886 nM staurosporine to induce apoptosis.
887 (C) As in (A) but 6-month-old WT and *Polg*^{D257A} macrophages were treated with 100
888 ng/ml TNFα, 500 nM Birinapant, and 20 μM zVAD-FMK to induce necrosis.
889 (D) As in (C) but with 12-month-old WT and *Polg*^{D257A} macrophages.
890 Statistical analysis: n=3 *$p < 0.05$, **$p < 0.01$, ***$p < 0.001$. Statistical significance deter-
891 mined for (A) using one-way ANOVA with Sidak's post-test and (B-D) using two-way
892 ANOVA with Tukey's post-test.

893

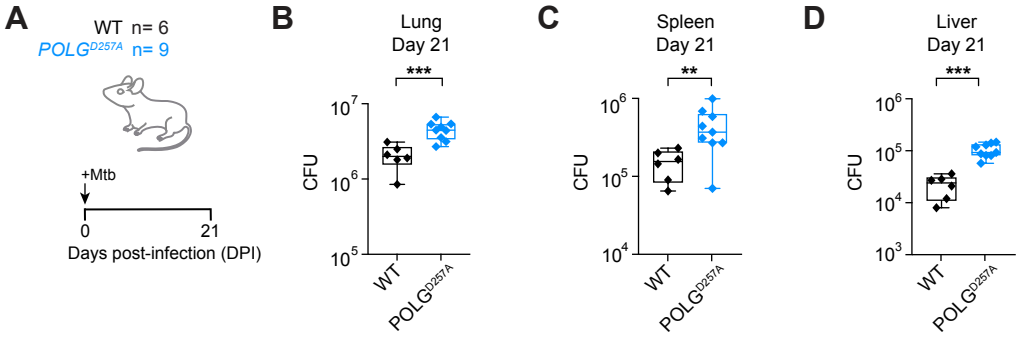
A
WT n= 6
POLGD257A n= 9
+Mtb
0
21
Days post-infection (DPI)
B
Lung
Day 21
***
CFU
10^7
10^6
10^5
WT
POLGD257A
C
Spleen
Day 21
**
CFU
10^6
10^5
10^4
WT
POLGD257A
D
Liver
Day 21
***
CFU
10^6
10^5
10^4
10^3
WT
POLGD257A

Figure 1

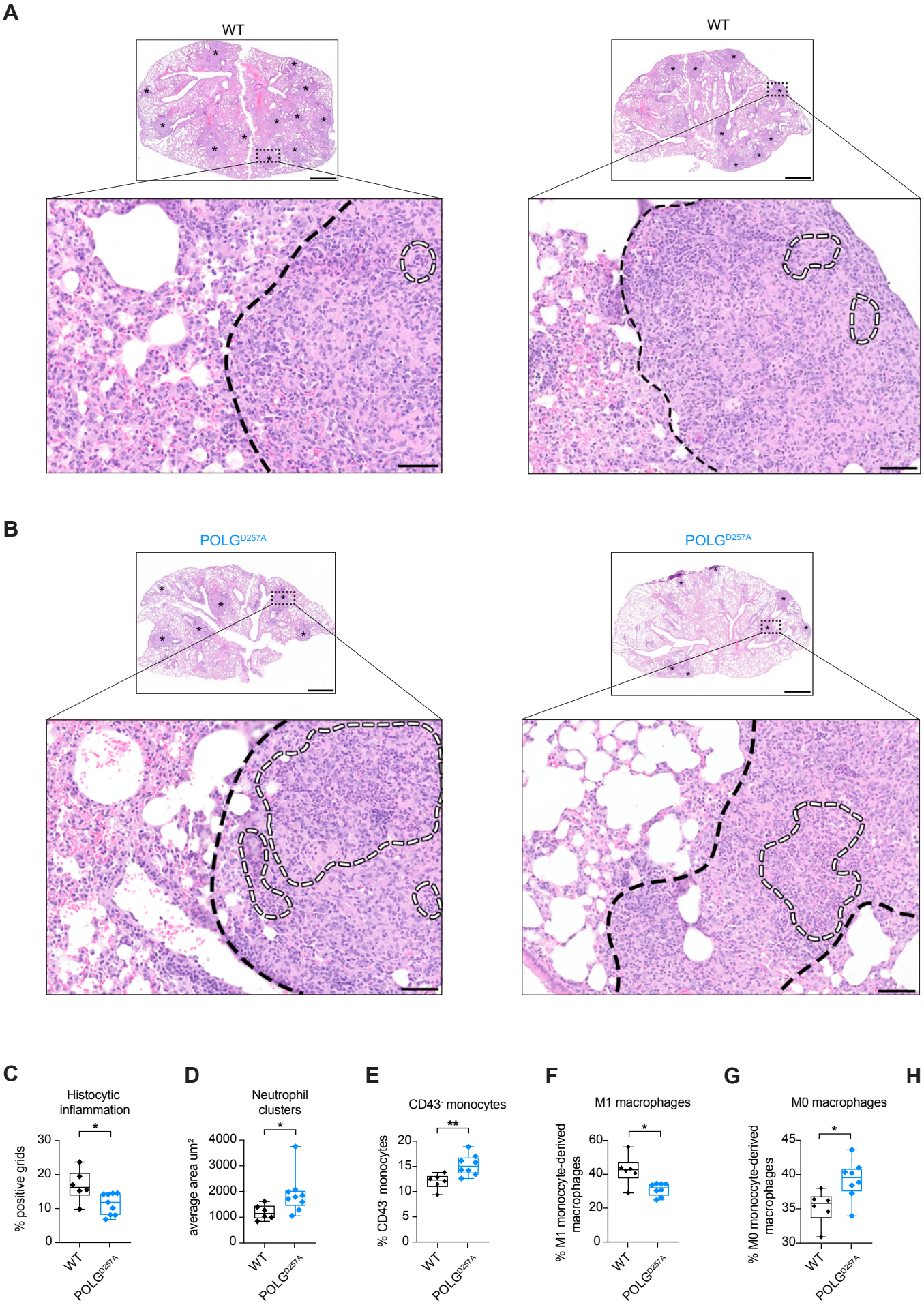
A
WT
WT
B
POLGD257A
POLGD257A
C
Histocytic inflammation
% positive grids
30
20
10
0
*
WT
POLGD257A
D
Neutrophil clusters
average area um2
4000
3000
2000
1000
0
*
WT
POLGD257A
E
CD43- monocytes
% CD43- monocytes
20
15
10
5
0
**
WT
POLGD257A
F
M1 macrophages
% M1 monoccyte-derived macrophages
60
40
20
0
*
WT
POLGD257A
G
M0 macrophages
% M0 monoccyte-derived macrophages
45
40
35
30
*
WT
POLGD257A
H
Neutrophils
% neutrophils
25
20
15
10
5
0
**
WT
POLGD257A

Figure 2

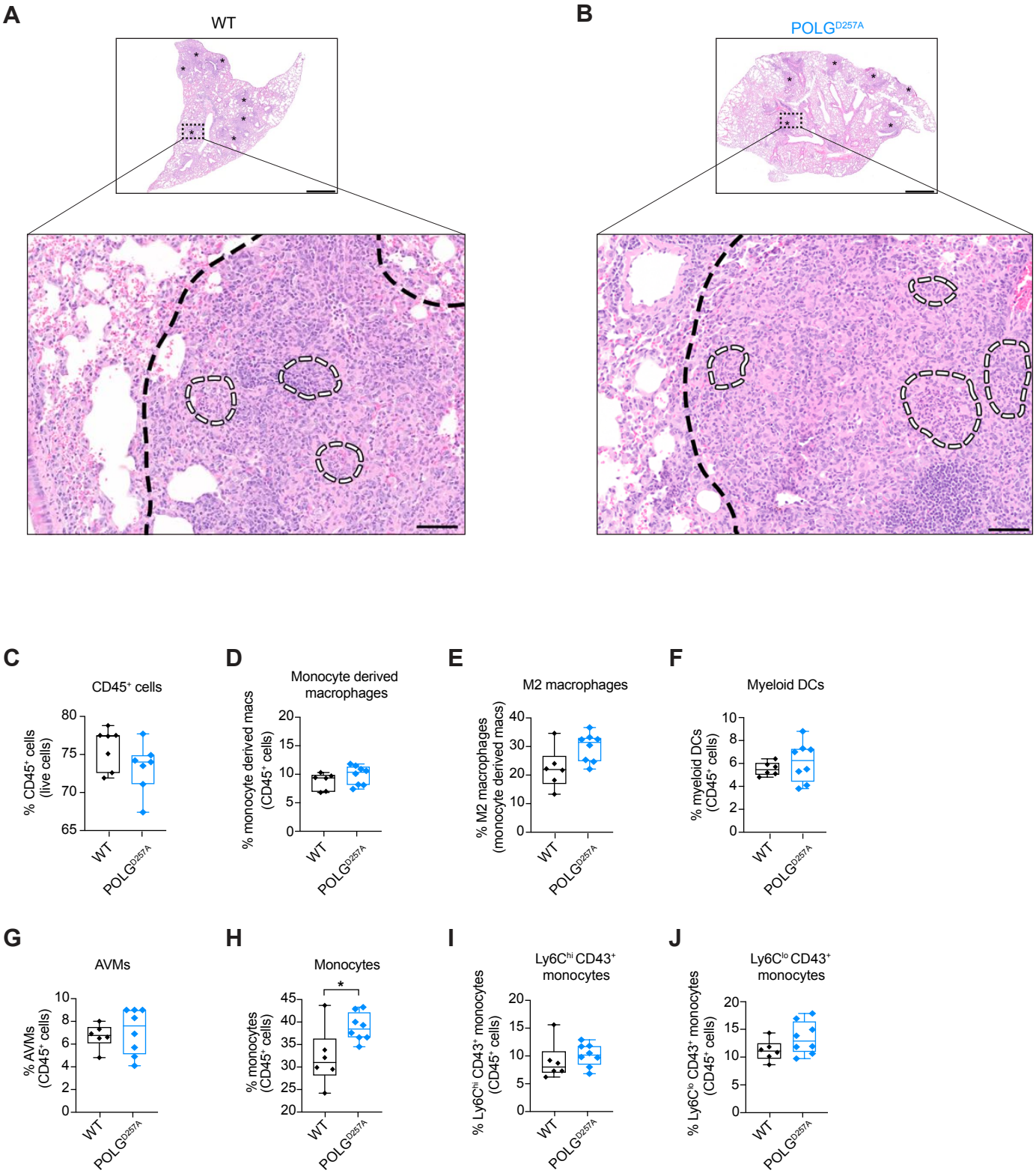
A
WT
B
POLGD257A
C
CD45+ cells
% CD45+ cells (live cells)
80
75
70
65
WT
POLGD257A
D
Monocyte derived macrophages
% monocyte derived macs (CD45+ cells)
20
15
10
5
0
WT
POLGD257A
E
M2 macrophages
% M2 macrophages (monocyte derived macs)
40
30
20
10
0
WT
POLGD257A
F
Myeloid DCs
% myeloid DCs (CD45+ cells)
10
8
6
4
2
0
WT
POLGD257A
G
AVMs
% AVMs (CD45+ cells)
10
8
6
4
2
0
WT
POLGD257A
H
Monocytes
*
% monocytes (CD45+ cells)
45
40
35
30
25
20
WT
POLGD257A
I
Ly6Chi CD43+ monocytes
% Ly6Chi CD43+ monocytes (CD45+ cells)
20
15
10
5
0
WT
POLGD257A
J
Ly6Clo CD43+ monocytes
% Ly6Clo CD43+ monocytes (CD45+ cells)
20
15
10
5
0
WT
POLGD257A

Figure S2

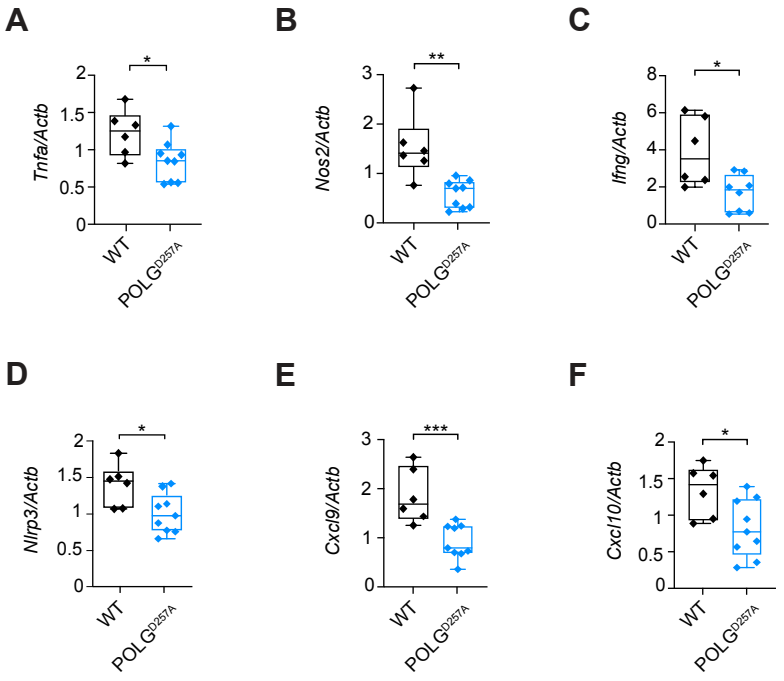
A
B
C
D
E
F
Tnfa/Actb
Nos2/Actb
Ifng/Actb
Nlrp3/Actb
Cxcl9/Actb
Cxcl10/Actb
WT
POLG D257A
*
**
***

Figure 3

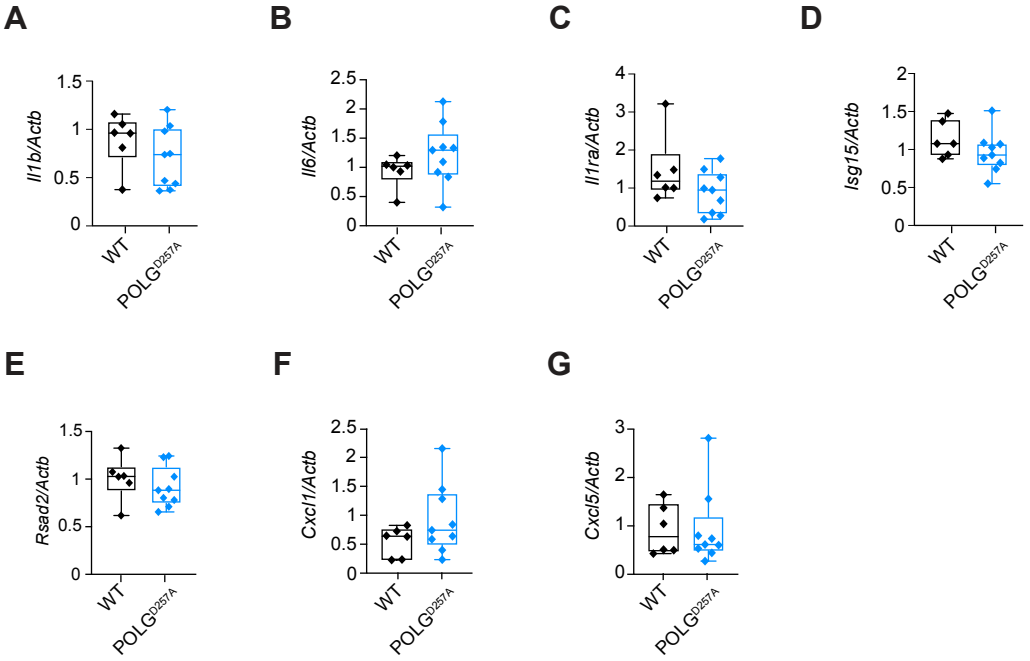
A
Il1b/Actb
1.5
1
0.5
0
WT
POLGD257A
B
Il6/Actb
2.5
2
1.5
1
0.5
0
WT
POLGD257A
C
Il1ra/Actb
4
3
2
1
0
WT
POLGD257A
D
Isg15/Actb
2
1.5
1
0.5
0
WT
POLGD257A
E
Rsad2/Actb
1.5
1
0.5
0
WT
POLGD257A
F
Cxcl1/Actb
2.5
2
1.5
1
0.5
0
WT
POLGD257A
G
Cxcl5/Actb
3
2
1
0
WT
POLGD257A

Figure S3

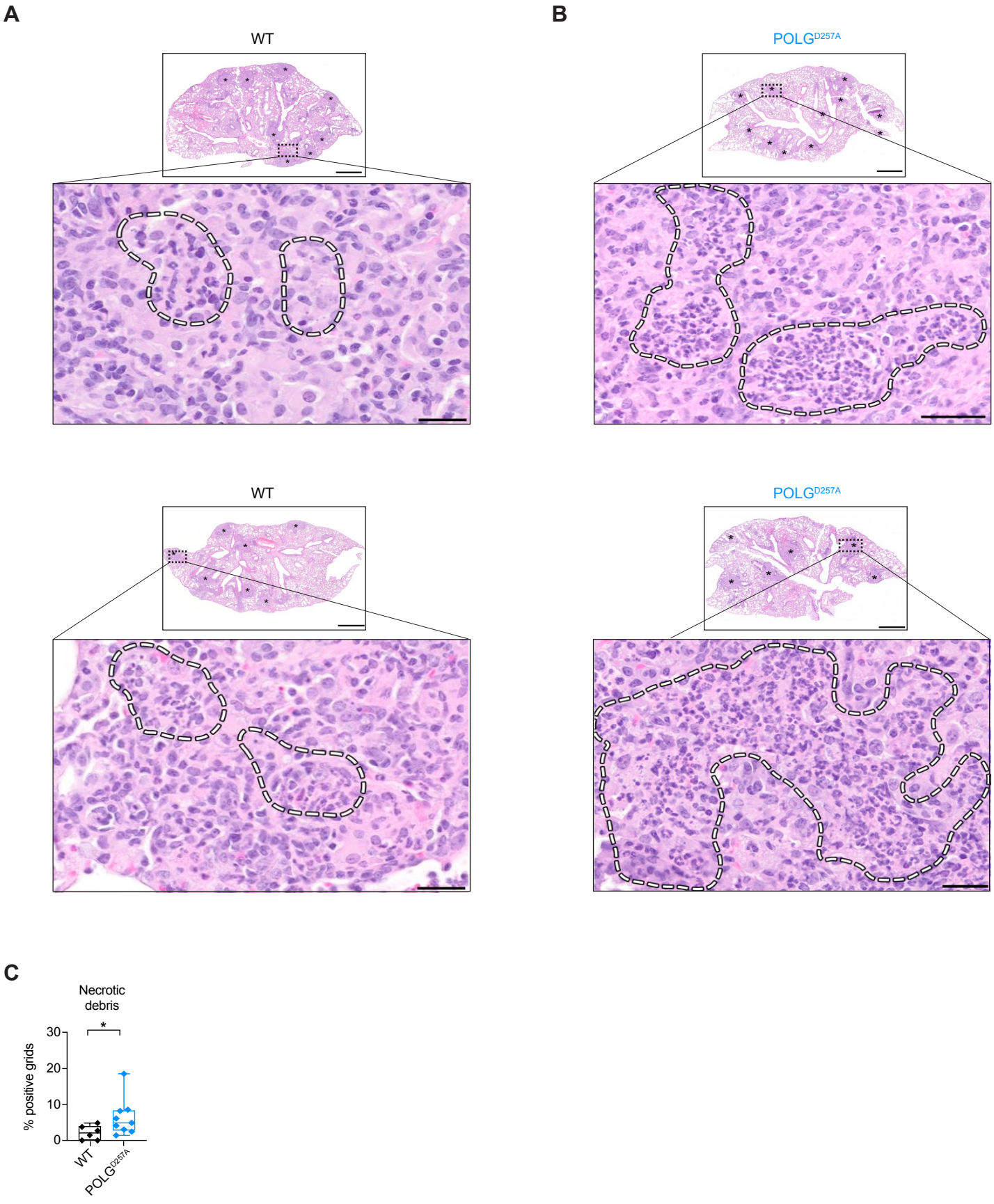
A
WT
B
POLGD257A
WT
POLGD257A
C
Necrotic debris
% positive grids
30
20
10
0
*
WT
POLGD257A

Figure 4

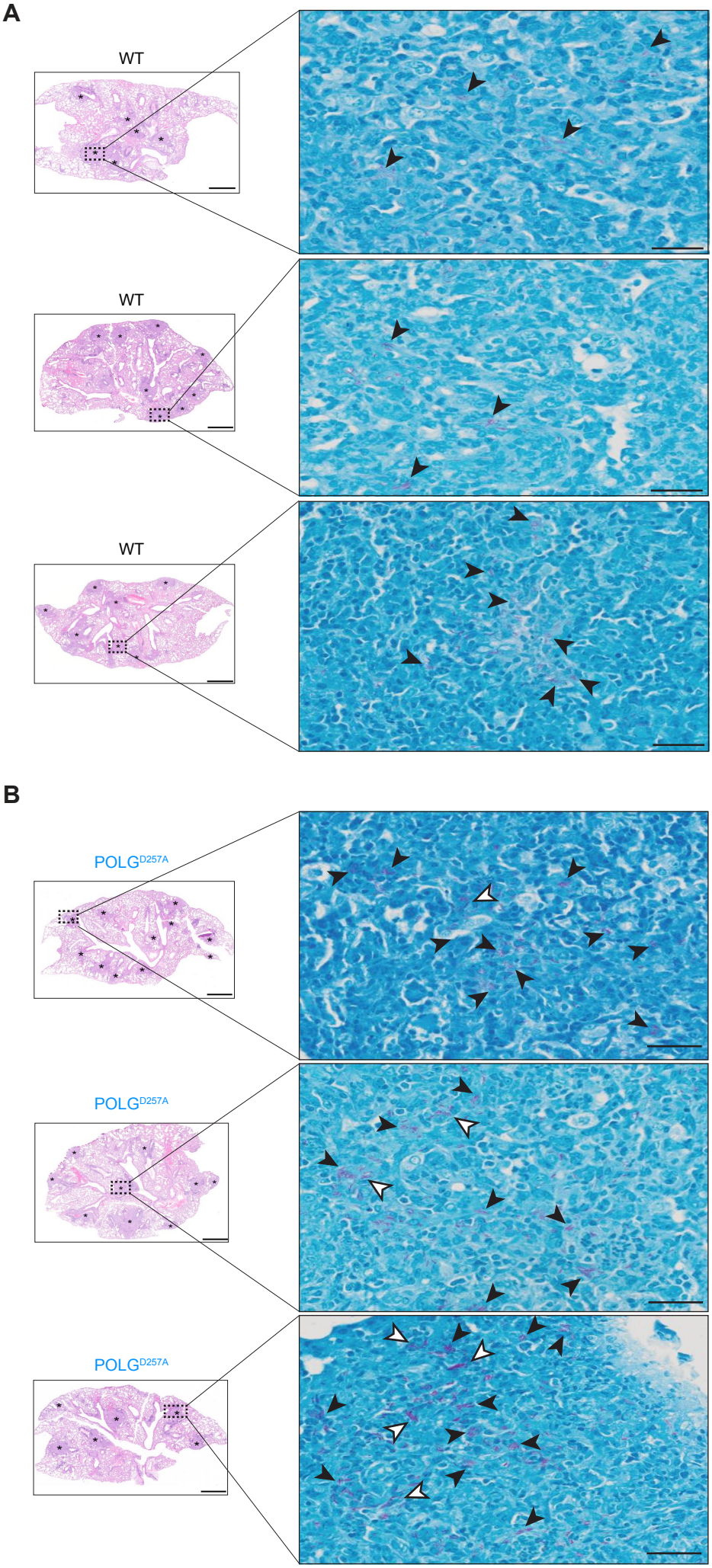

Figure 5

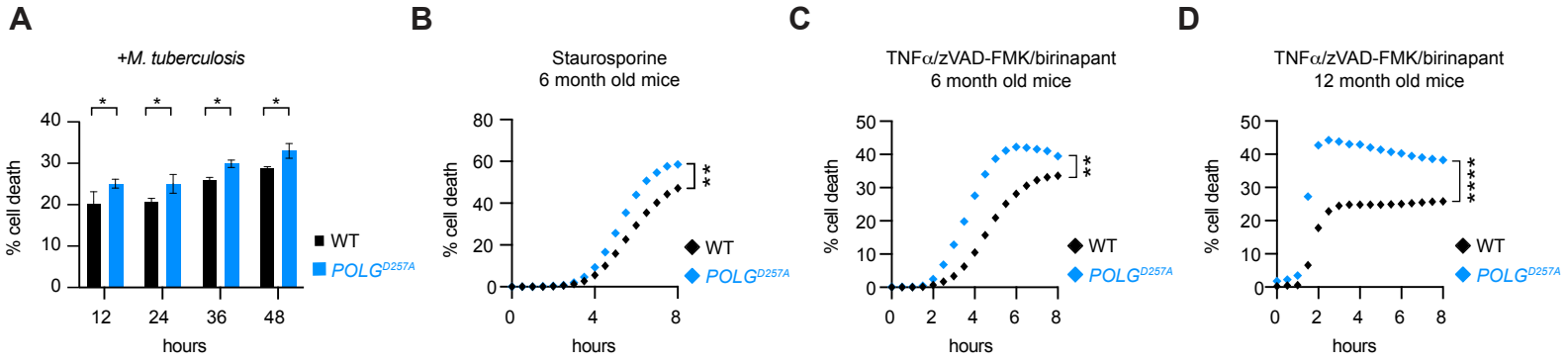
A
+M. tuberculosis
% cell death
hours
WT
POLG D257A
B
Staurosporine
6 month old mice
% cell death
hours
WT
POLG D257A
C
TNFα/zVAD-FMK/birinapant
6 month old mice
% cell death
hours
WT
POLG D257A
D
TNFα/zVAD-FMK/birinapant
12 month old mice
% cell death
hours
WT
POLG D257A

Figure 6